Monthly Notices
of the
ROYAL ASTRONOMICAL SOCIETY

MNRAS **429,** 2974–2985 (2013) doi:10.1093/mnras/sts545

Three-integral multicomponent dynamical models and simulations of the nuclear star cluster in NGC 4244

F. De Lorenzi,[1]★ M. Hartmann,[2] V. P. Debattista,[3]†‡ A. C. Seth[4] and O. Gerhard[5]

[1]*Zürcher Hochschule für Angewandte Wissenschaften, Technikumstrasse 9, CH-8401 Winterthur, Switzerland*
[2]*Astronomisches Rechen-Institut, Zentrum für Astronomie der Universität Heidelberg (ZAH), Mönchhofstr. 12-14, D-69120 Heidelberg, Germany*
[3]*Jeremiah Horrocks Institute, University of Central Lancashire, Preston, Lancashire, PR1 2HE*
[4]*University of Utah, Salt Lake City, UT, USA*
[5]*Max-Planck-Institut für extraterrestrische Physik, Giessenbachstraße, D-85741 Garching, Germany*

Accepted 2012 December 3. Received 2012 December 3; in original form 2012 August 10

ABSTRACT

Adaptive optics observations of the flattened nuclear star cluster in the nearby edge-on spiral galaxy NGC 4244 using the Gemini near-infrared integral field spectrograph (NIFS) have revealed clear rotation. Using these kinematics plus 2MASS photometry, we construct a series of axisymmetric two-component particle dynamical models with our improved version of NMAGIC, a flexible χ^2-made-to-measure code. The models consist of a nuclear cluster disc embedded within a spheroidal particle population. We find a mass for the nuclear star cluster of $M = 1.6^{+0.5}_{-0.2} \times 10^7\,\mathrm{M}_\odot$ within ∼42.4 pc (2 arcsec). We also explore the presence of an intermediate-mass black hole and show that models with a black hole as massive as $M_\bullet = 5.0 \times 10^5\,\mathrm{M}_\odot$ are consistent with the available data. Regardless of whether a black hole is present or not, the nuclear cluster is vertically anisotropic ($\beta_z < 0$), as was found with earlier anisotropic Jeans models. We then use the models as initial conditions for *N*-body simulations. These simulations show that the nuclear star cluster is stable against non-axisymmetric perturbations. We also explore the effect of the nuclear cluster accreting star clusters at various inclinations. Accretion of a star cluster with mass 13 per cent that of the nuclear cluster is already enough to destroy the vertical anisotropy, regardless of orbital inclination.

Key words: galaxies: formation – galaxies: individual: NGC 4244 – galaxies: kinematics and dynamics – galaxies: nuclei – galaxies: spiral – galaxies: star clusters: general.

1 INTRODUCTION

Studies of the centres of galaxies across the Hubble sequence have shown that they frequently host central massive objects such as massive nuclear star clusters (NCs) and supermassive black holes (SMBHs). NCs are present in roughly 75 per cent of low- and intermediate-luminosity disc and elliptical galaxies (Böker et al. 2002; Côté et al. 2006). These NCs are intrinsically very luminous, with typical $M_I \sim -12$, and sizes similar to globular clusters ($r_{\rm eff} \sim$ 5 pc; Böker et al. 2004).

Two hypotheses have been offered to explain NC formation. One scenario envisages NCs forming in situ out of gas cooling on to the centre (Milosavljević 2004; Bekki, Couch & Shioya 2006; Bekki 2007). Alternatively, NCs may form from star clusters (SCs) merging at the centres of galaxies (Tremaine, Ostriker & Spitzer 1975; Lotz et al. 2001; Capuzzo-Dolcetta & Miocchi 2008; Agarwal & Milosavljević 2011; Antonini et al. 2012; Antonini 2012). Which hypothesis is correct determines whether NC growth is limited by the supply of SCs from the host galaxy (Antonini 2012) or regulated by feedback from in situ star formation (McLaughlin, King & Nayakshin 2006).

The assembly history of NCs can be constrained from their morphology, stellar populations and kinematics. In late-type spirals, NCs have been found to consist of multiple stellar populations, typically a young population (<100 Myr), and a dominant population older than 1 Gyr (Davidge & Courteau 2002; Schinnerer, Böker & Meier 2003; Rossa et al. 2006; Walcher et al. 2006). The *Hubble Space Telescope* (*HST*) has revealed that the NCs of edge-on galaxies host multiple stellar populations associated with different morphological components (Seth et al. 2006). These NCs consist of young blue nuclear cluster discs (NCD) and older nuclear cluster spheroids (NCS). Optical spectra of the NC in the edge-on Scd

★ E-mail: flavio.delorenzi@gmx.ch
† RCUK Academic Fellow.
‡ Visiting Lecturer, Department of Physics, University of Malta, Tal-Qroqq Street, Msida, MSD 2080, Malta.

galaxy NGC 4244 ($i \approx 90^\circ$), the nearest galaxy in the sample of Seth et al. (2006) ($D = 4.37$ Mpc; Seth, Dalcanton & de Jong 2005a), indicates the presence of multiple stellar populations, while near-infrared spectroscopy showed that the NC is rapidly rotating (Seth et al. 2008b). Using *N*-body simulations, Hartmann et al. (2011, hereafter H11) showed that the NC in NGC 4244 cannot have assembled more than half its mass via the accretion of SCs.

NCs exhibit several scaling relations. The luminosity of NCs correlates with that of their host galaxy (Böker et al. 2002; Côté et al. 2006; Erwin & Gadotti 2010). A number of studies also found that their mass, $M_{\rm NC}$, correlates with the velocity dispersion of the host bulge, the $M_{\rm NC}$–σ relation (Ferrarese et al. 2006; Rossa et al. 2006; Wehner & Harris 2006). Early work found that this $M_{\rm NC}$–σ relation is parallel to the $M_\bullet$–σ relation of SMBHs (Ferrarese & Merritt 2000; Gebhardt et al. 2000), with NCs being about ten times more massive, at the same σ, as SMBHs. However, recent work has questioned how comparable NCs and SMBHs are. Erwin & Gadotti (2012) find that NCs and SMBHs follow different relations, with SMBH masses correlated with properties of the bulge, while NCs seem to correlate better with properties of the entire host galaxy. Instead, both Leigh, Böker & Knigge (2012) and Scott & Graham (2012) show that there is an $M_{\rm NC}$–σ relation but with a significantly different slope than for SMBHs. It is not clear at present whether these differences are intrinsic to NC and SMBH growth or whether they are due to the fact that the scaling relations depend on Hubble type. In particular, some recent studies have suggested that SMBHs and NCs in late-type galaxies do not follow the same scaling relations as in early types (Greene et al. 2010; Erwin & Gadotti 2012). Some galaxies host both an NC and an SMBH (Seth et al. 2008a; Graham & Spitler 2009). The relative properties of NCs and SMBHs in such galaxies could constrain the relationship between these objects. For instance, by constructing an ($M_\bullet + M_{\rm NC}$)–σ relation which includes the mass of both the NC and of the SMBH (Graham et al. 2011), Graham (2012) found a flatter relation than the $M_\bullet$–σ relation. But the small existing sample of objects with known NCs and SMBHs is currently too small to obtain a clear picture (e.g. Neumayer & Walcher 2012). Progress in determining whether NCs and SMBHs are related therefore requires improving the statistics of such measurements. Moreover, a better understanding of the mass assembly of NCs in late-type galaxies is vital.

It is generally thought that AGN feedback is responsible for the $M_\bullet$–σ relation (e.g. Silk & Rees 1998; King 2003; Di Matteo, Springel & Hernquist 2005; Murray, Quataert & Thompson 2005; Sazonov et al. 2005; Springel, Di Matteo & Hernquist 2005; Johansson, Naab & Burkert 2009), but scenarios where this relation arises because the galaxy regulates SMBH growth (e.g. Burkert & Silk 2001; Kazantzidis et al. 2005; Miralda-Escudé & Kollmeier 2005) or purely indirectly by the hierarchical assembly through galaxy merging (Haehnelt & Kauffmann 2000; Adams, Graff & Richstone 2001; Adams et al. 2003; Jahnke & Macciò 2011) have also been proposed. If gas inflow plays a more important role in the growth of NCs then this opens the possibility that some form of feedback drives the scaling relations in both SMBHs and NCs (e.g. McLaughlin et al. 2006).

To help shed light on the formation of NCs in late-type galaxies, in this paper we study the NC in the nearby Sc galaxy NGC 4244. H11 modelled this NC using anisotropic JAM models (Cappellari 2008), obtaining a mass of $(1.1 \pm 0.2) \times 10^7\,{\rm M}_\odot$. In this paper, we build three-integral particle models of the same NC and use them as initial conditions for *N*-body simulations to explore its sensitivity to SC accretion. The outline of this paper is as follows. Section 2 describes the observational data and how they are used in the dynamical modelling. Our modelling method, the χ^2-M2M code NMAGIC based on de Lorenzi et al. (2007, 2008, 2009), is described in Section 3 including additional code development. We construct various axisymmetric particle models of the nuclear region of NGC 4244 in Section 4 using this improved code. The models consist of an NCD and an NCS having separate mass-to-light (M/L) ratios. Using the best model as initial conditions for *N*-body simulations, we explore the evolution of the NC in Section 5. Section 6 discusses our results in the context of NC formation.

2 OBSERVATIONAL DATA

We begin by describing the photometry and how these data are deprojected to obtain a three-dimensional luminosity density. After this, the integral-field kinematic data are presented. We adopt a distance to NGC 4244 of 4.37 Mpc (Seth, Dalcanton & de Jong 2005b). At this assumed distance, 1 arcsec corresponds to 21 pc.

2.1 Photometry

Here, we give a brief summary of the photometric data and its model representation, both described in detail in Seth et al. (2005a, 2008b).

The photometry consists of *K*-band data either from 2MASS or from the near-infrared integral field spectrograph (NIFS) observations of Seth et al. (2008b). The main disc (MD) of NGC 4244 hosts at its centre an NC which is composed of an NCD and an oblate NCS. The *K*-band mass-to-light ratio M/L_K is estimated to be 0.5–0.75 for the galaxy as a whole [from integrated colours taken from LEDA [$B - V = 0.4$–0.6] combined with M/L from Bell et al. (2003)]. The M/L_K of the NCD is in the range 0.1–0.25 based on Bruzual & Charlot (2003) models applied to the optical spectroscopy of Seth et al. (2006), which agrees well with the fitted luminosities for the disc in *HST*/ACS and NIFS bands. The NCS stellar populations are poorly constrained and an M/L_K between 0.5 and 1.2 is likely.

The surface brightness of NGC 4244 is decomposed into an axisymmetric three-component model. The luminosity distributions of the MD and the NCD are modelled as projected edge-on exponential discs (e.g. van der Kruit & Searle 1981):

$$\Sigma(x, z) = \Sigma_0 \left(\frac{x}{h_r}\right) K_1(x/h_r)\,\mathrm{sech}(z/z_0)^2, \quad (1)$$

where Σ_0 and h_r are constants, and K_1 is the modified Bessel function. The corresponding model parameters for the MD and NCD models are taken from Seth et al. (2005a) and Seth et al. (2008b), respectively.

On the other hand, the NCS is represented using a Sérsic (1968) profile:

$$I(x, z) = I_e \exp\left(-b_n((R/R_e)^{1/n} - 1)\right), \quad (2)$$

where I_e is the surface brightness at the effective radius R_e, $b_n \simeq 1.992n - 0.3271$ and $R = \sqrt{x^2 + (z/q)^2}$ is the elliptical radius, with flattening q. Best-fitting parameters have been obtained from Seth et al. (2008b).

All models were convolved with a Gaussian point spread function (PSF) of 0.23 arcsec FWHM during the fitting process, cf. Seth et al. (2008b). The best-fitting parameters are summarized in Table 1. The left-hand panel of Fig. 1, which presents the NCS model, shows its surface brightness, μ_K, and ellipticity, $\epsilon = 1 - q$, profiles.

Table 1. Best-fitting parameters of the photometric three-component model taken from Seth et al. (2005a, 2008b). The model consists of an exponential main disc (MD), an exponential nuclear cluster disc (NCD) and a Sérsic nuclear cluster spheroid (NCS).

Comp.	Σ_0 ($L_\odot$ pc^{-2})	ρ_0 ($L_\odot$ pc^{-3})	h_r (pc)	z_0 (pc)	q	I_e ($L_\odot$ pc^{-2})	R_e (pc)	n
MD	598	0.167	1783	469				
NCD	1.41×10^5	2.08×10^4	3.39	1.19				
NCS					0.81	8.73×10^3	10.86	1.68

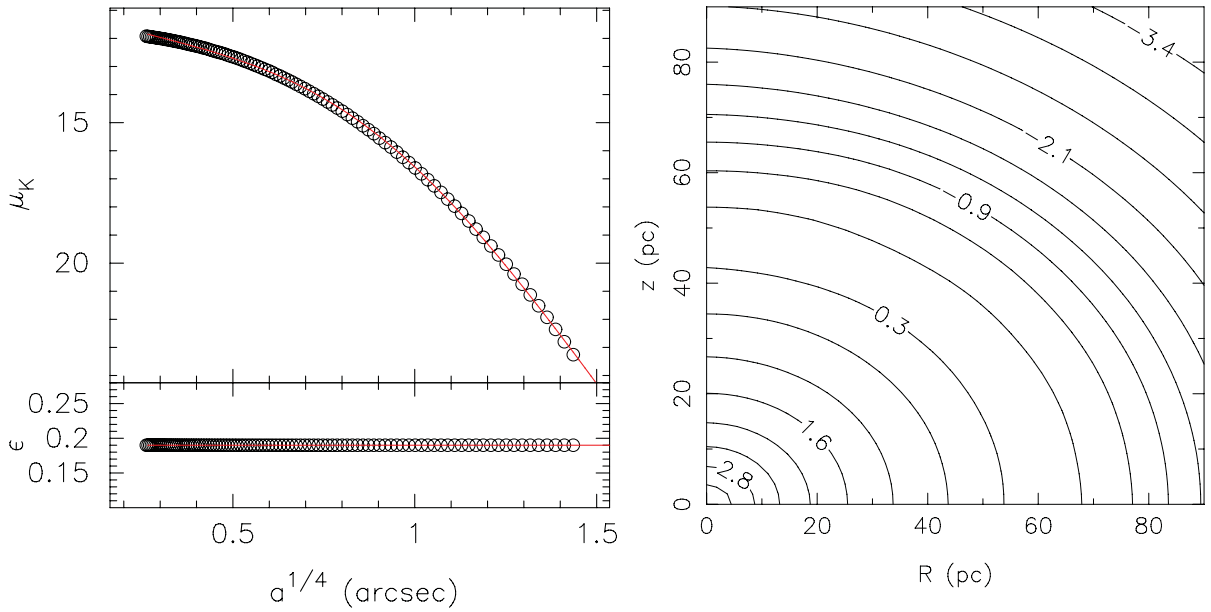

Figure 1. Left: comparison of the NCS Sérsic photometry with the reprojected three-dimensional luminosity model. The data points correspond to the NCS Sérsic profile, which was derived via a morphological fit. The solid line shows the model projected on to the sky plane. The upper panel shows the surface brightness, μ_K, and the lower one shows the ellipticity, $\epsilon = 1 - q$. Right: isodensity contours of the NCS in the meridional plane. The luminosity density was obtained by an edge-on deprojection of the NCS Sérsic surface brightness. The contour labels are given in units of $\log_{10} L_\odot$ pc^{-3}.

2.1.1 Deprojection

To compute the three-dimensional luminosity distribution, each component of the surface brightness model is deprojected individually. The edge-on deprojection of an axisymmetric system is unique (Rybicki 1987). The surface brightness profile of equation (1) corresponds to an exponential disc, so the deprojection is readily given by (e.g. van der Kruit & Searle 1981)

$$\rho(R, z) = \rho_0 \exp(-R/h_r)\,\mathrm{sech}(z/z_0)^2, \quad (3)$$

where $\rho_0 = \Sigma_0/(2h_r)$, and Σ_0, h_r and z_0 are the same as in equation (1). Their values are given in Table 1.

Unlike the surface brightness profile of an exponential disc, the Sérsic profile of the NCS cannot be deprojected in closed form. We therefore use the program of Magorrian (1999) to numerically deproject the surface brightness distribution of the NCS. The program finds a smooth axisymmetric density distribution consistent with the surface brightness distribution for the specified inclination angle (here edge-on, i.e. 90°), by imposing that the solution maximizes a penalized likelihood. Because the deprojection is computed numerically and tabulated on a grid, the reprojected surface brightness profile may not match the Sérsic one perfectly. A comparison of the NCS Sérsic photometric model and its edge-on deprojection reprojected on to the sky plane, seen in the left-hand panel of Fig. 1, shows that the numerical deprojection is in fact very reliable. The right-hand panel presents isodensity contours in the meridional plane of the NCS obtained with the Magorrian (1999) code.

2.2 Kinematic data

The integral-field NIFS kinematic data we use in the modelling were presented in Seth et al. (2008b) and consist of velocity, velocity dispersion and the higher order Gauss–Hermite moments h_3 and h_4 (Gerhard 1993; van der Marel & Franx 1993). The NIFS field-of-view extends to ±1.5 arcsec along each direction, but the usable data are within ±1.0 arcsec. In this field-of-view, the positions of the 'spaxels' within which spectra were taken define a grid of 63 × 71 = 4473 cells, which serves as the basis grid for Voronoi bins for which the velocity, velocity dispersions, h_3 and h_4 are given.

3 METHODS

We construct a range of dynamical models for the NC of NGC 4244. These models consist of a disc and a spheroidal particle population representing the NCD and NCS, respectively. We use an adapted version of the flexible χ^2-made-to-measure (M2M) particle code NMAGIC described in de Lorenzi et al. (2007, 2008). This section describes a few ingredients required to construct dynamical M2M models and presents further development of NMAGIC compared with our previous work in de Lorenzi et al. (2007, 2008).

3.1 Model observables

The central luminosity volume density of the NCS is about a million times larger than that of the MD (Seth et al. 2008b). Thus, the NCS dominates the luminosity distribution in the central region out to the edge of the observational data, allowing us to neglect the luminosity distribution of the MD when computing the photometric observables. At a distance $R = 30$ pc from the centre, the luminosity density in the equatorial plane of the NCS is still about 100 times that of the MD.

We compute separate spherical harmonic coefficients A_{lm} for the density of the NCD and the NCS. The corresponding errors are inferred following a Monte Carlo procedure described in de Lorenzi et al. (2008), in which the A_{lm}'s are computed many times from random rotations about arbitrary axes of a suitable particle realization. Here, we used the isotropic particle model generated from the major-axis density profiles of the NCS and NCD components, described in Section 3.2 below. The $A_{lm}^{\rm NCD}$ and $A_{lm}^{\rm NCS}$ constrain the photometry of the disc and spheroidal particle populations, respectively. We use even A_{lm}'s up to $l_{\rm max} = 8$ in 40 radial bins, unevenly spaced, for a total of $N_{Alm} = 2000$ photometric constraints. The grid starts at $r_{\rm min} = 0.0001$ arcsec (0.002 pc) and extends to $r_{\rm max} = 2$ arcsec (42.4 pc).

The NIFS kinematic data (velocity v, dispersion σ, h_3 and h_4) are bi-symmetrized by adopting a point-symmetric reflection with respect to the centre of the galaxy, as described in de Lorenzi et al. (2009), followed by a reflection about the major axis. The resulting data within ± 0.7 arcsec are shown in the upper panel of Fig. 6. As kinematic observables we use luminosity-weighted Gauss–Hermite coefficients h_1 up to h_4 (Gerhard 1993; van der Marel & Franx 1993; de Lorenzi et al. 2008) and the luminosity itself (corresponding to h_0) within the field of view, for a total of $N_{\rm kin} = 365$ kinematic observables (73 Voronoi bins times 5 sets of Gauss–Hermite coefficients). These are used to constrain the particle system as a whole, without distinguishing between NCD and NCS populations. The particle model is seeing convolved with a Gaussian PSF having an FWHM of 0.23 arcsec (5 pc) by means of the Monte Carlo method presented in de Lorenzi et al. (2008): when the model kinematics are computed, each particle is temporarily replaced by $N_{\rm pp}$ pseudo particles with randomly selected positions having probabilities given by the PSF. In this work, we adopted $N_{\rm pp} = 5$.

3.2 Initial conditions

We set up *spherical* initial conditions using the major-axis density profile of the NCS. Setting $M/L_K = 1$, the mass density is normalized to unit mass and the self-consistent gravitational potential is computed. Following Gerhard (1991), the isotropic distribution function is computed and used to generate a set of equal mass particles as in Debattista & Sellwood (2000). Finally, 30 per cent of the particles are randomly assigned to the 'disc' population. We produced two realizations of these initial conditions, a low resolution one with 0.75M particles which allowed us to explore parameter space quickly and a higher resolution version with 6M particles.

3.3 Gravitational potential

The M2M method works by adjusting the weights of individual particles while they are evolved along their orbits. For this orbit integration, the gravitational potential of the system is needed. This section details the methods used to construct the dynamical models presented in Section 4 below. In brief, low-resolution models (M1) are built using an FFT method for the potential. Then high-resolution models without (M2) and with intermediate-mass black holes (IMBHs) (M3–M8) are built with the potential computed on a spherical mesh of spherical harmonics (Sellwood 2003).

We assume that the mass distributions of the MD, NCD and NCS follow their luminosity distributions J_i ($i \in \{\rm MD, NCD, NCS\}$). For a constant mass-to-light ratio M/L_i, the corresponding mass density is $\rho_i = (M/L_i)J_i$, with J_i the deprojection given in Section 2.1.1.

The potential in models M1 was obtained on a Cartesian grid. Each Cartesian grid consists of $N = 128^3$ grid cells. The NC grid extends to ± 50 pc along each direction, whereas the MD grid extends to ± 3000 pc. This allows us to resolve the scaleheights of the MD and the NCD, and the half-mass radius of the NCS. The potential on each grid is calculated using the Fourier convolution theorem. We assign to each mesh point a mass from the corresponding density distribution. The potential is then obtained by a convolution with the Greens function. We employ the FFT method of Press et al. (1992) to perform the convolution.

We pre-compute the individual gravitational potentials Φ_i^{M1} generated by J_i, for unit mass-to-light ratio. This procedure allows us to quickly obtain the total gravitational potential for any choice of M/L_i through a weighted sum $\Phi = \sum_i M/L_i \Phi_i^{M1}$, which is kept constant for each model run.

For a modelling run, we initially tabulate $\Phi_i = M/L_i \Phi_i^{M1}$ on individual Cartesian grids. Forces at grid points are computed by finite differences. Individual particle accelerations are then approximated by a cloud-in-cell scheme (Hockney & Eastwood 1988) to interpolate the grid point forces to the particle position.

For models in the series M2–M8, we use a spherical harmonic potential solver as described in Sellwood (2003). We use the disc and spheroid particle populations (particle weights are converted to mass via the associated M/L_K) to calculate the gravitational potential of the entire particle system. Thus, the contribution of the MD is neglected. As discussed at the end of Section 2.1.1, the error associated with this approximation is expected to be very small. For models using the spherical harmonic potential solver, the potential is updated after every M2M correction step (and temporally smoothed). We use potential expansion coefficients up to $l_{\rm max} = 8$ with 300 (unevenly spaced) radial bins to $r_{\rm max} = 200$ pc. The width of the innermost bin is 0.2 pc and of the outermost bin is 4.2 pc, which is still smaller than the FWHM of the PSF.

3.4 Re-sampling a particle model

We use the final particle dynamical model as initial conditions for N-body simulations. In order to do this, it is best that the particles have a narrow range of masses; this ensures both higher effective mass resolution and a lower artificial two-body relaxation rate. The models are therefore built using the re-sampling technique described by Dehnen (2009). This section closely follows Dehnen (2009) work. We generate the models using a flat weight prior $\hat{w} = N^{-1}$. The particle models are re-sampled every 100 M2M correction steps if the ratio of largest to smallest particle weight is $\max\{w_i\}/\min\{w_i\} > 10$. Because we do not normalize total weight (it is only constrained by the observables, in particular by A_{00}), the weight of a re-sampled particle is set to $w_k = N^{-1} \sum_k w_{i,\rm old}$. The phase-space coordinates $(\boldsymbol{x}_k, \boldsymbol{y}_k)$ of the kth re-sampled orbit are set to the ith original trajectory if

$$C_i < \bar{\gamma}(k - 1/2) \le C_{i+1}, \qquad i, k \in [1, N] \tag{4}$$

with mean relative normalized weight $\bar{\gamma} = N^{-1} \sum_i \gamma_i$, cumulative relative normalized weight $C_i = \sum_{k<i} \gamma_k$ and $\gamma_i = w_i/\hat{w}$ the

relative weight. Orbits with $\gamma_i < \bar{\gamma}$ are re-sampled at most once, whereas orbits with $\gamma_i > \bar{\gamma}$ produce at least one copy. If a trajectory gets re-sampled, the first copy gets the phase-space position of the original particle. For additional copies, we randomize positions $(x \pm d, y \pm d, z \pm d)$ with $d = (x^2 + y^2)^{1/2}/100$ exploring the eight distinct combinations of plus and minus signs. The position of any additional copy is set to $(x + r_x d, y + r_y d, z + r_z d)$ with $r_{x,\,y,\,z} \in [-1, 1]$ uniform random numbers. We do not alter velocities and every copy keeps the velocity of the original particle. At small radii, $r < 0.2$ pc, we rotate the particles randomly about the z-axis otherwise the resulting orbits are too closely spaced. Our implementation of re-sampling conserves total particle number but not individually for the NCD and NCS. When a particle is re-sampled more than once all daughter particles inherit its affiliation to either the NCD or the NCS.

Particle re-sampling at work is illustrated in Fig. 2. The top panel compares a final particle weight distribution of a model generated using NMAGIC without re-sampling with the peaked distribution of a corresponding model built including re-sampling. The model with a narrow weight distribution has a higher effective resolution and hence suffers less from shot noise than its counterpart with a broad distribution. The effective number of particles is defined as $N_{\rm eff}/N = \overline{w}^2/\overline{w^2}$ (de Lorenzi et al. 2007). Then, the particle models shown in Fig. 2 have $1 - N_{\rm eff}/N = 0.67$ without re-sampling and $1 - N_{\rm eff}/N = 9.8 \times 10^{-6}$ with re-sampling, i.e. re-sampling leads to an approximately three times higher $N_{\rm eff}$. Starting from a spherical particle population, the NCD shown in the bottom panel is obtained by combining NMAGIC with re-sampling.

3.5 Run parameters

Based on our experience in previous work, we set the value of the force-of-change parameter $\epsilon = 8 \times 10^{-8}$ and the temporal smoothing parameter $\alpha = 2.1\epsilon$. We set the entropy parameter $\mu = 2 \times 10^{-6}$. [The parameters (ϵ, α, μ) are defined in Syer & Tremaine (1996) and de Lorenzi et al. (2009).] We used time-steps $\delta t = 673$ yr, with χ^2-M2M correction steps every 20 time-steps. For comparison, a circular orbit at $r = 13.4$ pc, which contains half the particle mass, takes 1.82 Myr.

4 DYNAMICAL MODELS

In this section, we construct dynamical models for the central region of NGC 4244 to assess its intrinsic kinematics and to constrain the NC mass. We investigate axisymmetric, two-component models for different combinations of mass-to-light ratios, fitting the photometry and NIFS integral-field kinematic data.

All models are constructed including re-sampling of particle coordinates as described in Section 3.4. In order to reduce computational cost, the bulk of the modelling is performed using 0.75M particles, with the gravitational potential calculated on the Cartesian grids and held fixed throughout. In these models, trajectories are integrated with a standard leapfrog scheme with a fixed time-step. The models are constructed in a two-step process. First, we start with the spherical isotropic 0.75M particle model and evolve it using NMAGIC to generate a particle realization with desired luminosity distribution, fitting simultaneously but separately the NCS and NCD photometric constraints. Since only photometric (not kinematic) constraints are fitted at this stage, the velocity scaling is arbitrary and only the ratio of $M/L_{\rm NCD}$ and $M/L_{\rm NCS}$ matters for the shape of the gravitational potential. In order to compute the gravitational potential the ratio $(M/L_{\rm NCD})/(M/L_{\rm NCS})$ is fixed at 0.2/1.8. The resulting

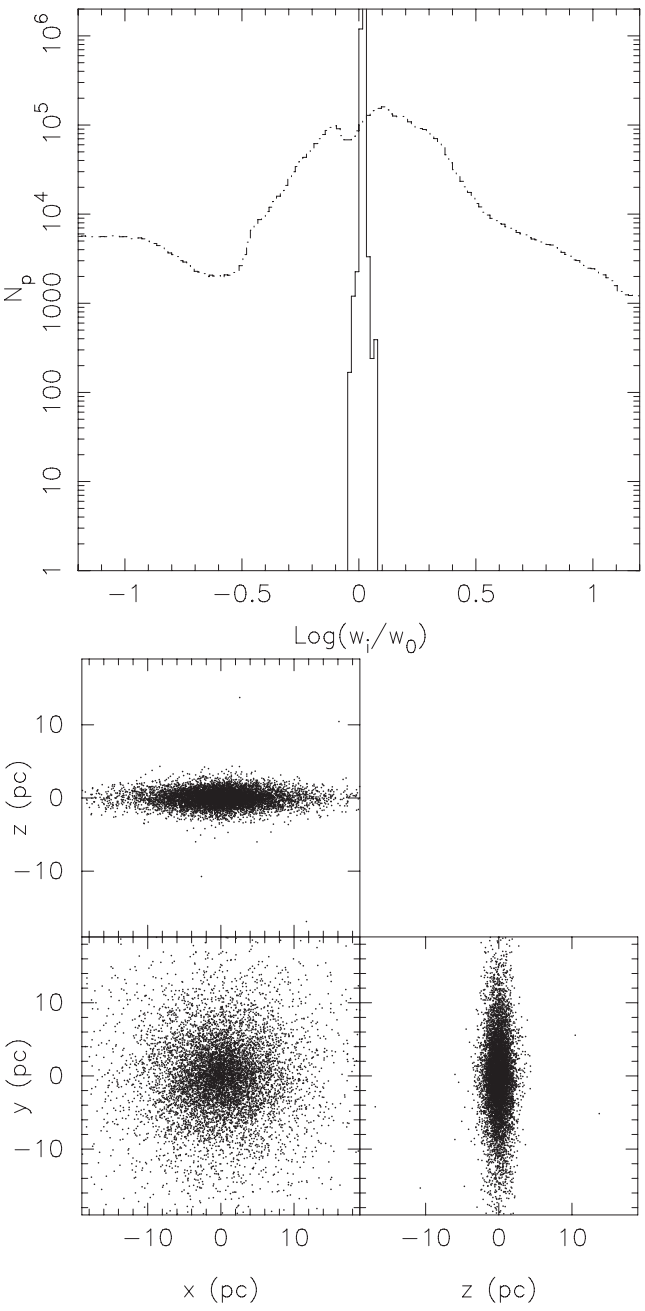

Figure 2. Top: comparison of the particle weight distribution of model M2 generated including re-sampling (solid line) and a corresponding model produced without re-sampling (dot–dashed line). Bottom: distribution of a subset of NCD particles of the M2 model, generated using NMAGIC with re-sampling. The three panels show different projections of the particle coordinates. Note that the initial NCD model was spherical.

model then serves as a starting point to simultaneously fit both the photometric and kinematic constraints ($N_{\rm obs} = 2365$ observables) for different combinations of $M/L_{\rm NCD}$ and $M/L_{\rm NCS}$. During this adjustment phase, we typically evolve for 4M time-steps (2.7 Gyr) and apply 200k M2M correction steps. The particle system is then relaxed for a further 100k time-steps (67 Myr) without changing particle weights. We refer to the final models as series M1. We vary $M/L_{\rm NCS}$ between 1.0 and 4.8, whereas we use values for $M/L_{\rm NCD}$ of 0.1, 0.2 and 0.4. The influence of the mass-to-light ratio of the MD on the quality of the fit is expected to be negligible; we therefore

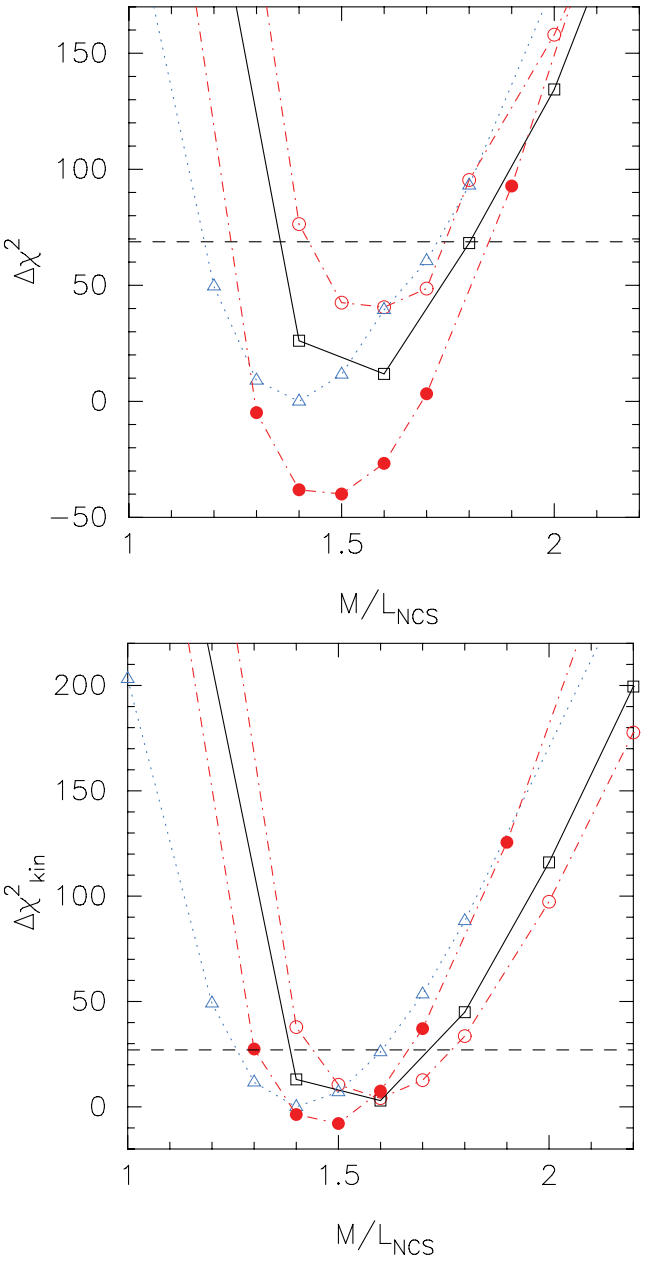

Figure 3. $\Delta\chi^2 = \chi^2 - \min\{\chi^2\}$ as a function of NCS and NCD *K*-band mass-to-light ratio. Upper panel: total $\Delta\chi^2$ for the model fitted to the photometric and kinematic target observables. Bottom panel: $\Delta\chi^2_{\rm kin}$ of the kinematic observables only. The dashed horizontal lines correspond to 68 per cent (1σ) confidence after van den Bosch & van de Ven (2009). The symbols are as follows: the M1 series for $M/L_{\rm NCD} = 0.1$, 0.2 and 0.4 are shown as open (red) circles, (black) squares and (blue) triangles, joined by dot–dashed, solid and dotted lines, respectively. Models in series M2 are indicated by the solid circles joined by the red dot–dashed lines.

keep it constant at $M/L_{\rm MD} = 0.7$ compatible with estimates from integrated colours.

The results are presented in Fig. 3, which illustrates how the quality of the model fit changes with mass-to-light ratios. The top panel shows $\Delta\chi^2 = \chi^2 - \min\{\chi^2\}$, whereas $\Delta\chi^2_{\rm kin}$ of the kinematic observables alone ($\Delta\chi^2$ 'marginalized' over the A_{lm}'s) is shown in the bottom panel. The 68 per cent confidence limits (1σ) are computed as $\sqrt{2N_{\rm obs}}$ following van den Bosch & van de Ven (2009). These limits are $\Delta\chi^2 = 68.8$ and $\Delta\chi^2_{\rm kin} = 27.0$, respectively.

Regardless of whether $\Delta\chi^2_{\rm kin}$ or $\Delta\chi^2$ is used, the resulting best model has mass-to-light ratios $M/L_{\rm NCD} = 0.4$ and $M/L_{\rm NCS} = 1.4$. Note that the models with $M/L_{\rm NCD} = 0.1$ or $M/L_{\rm NCD} = 0.2$ and $M/L_{\rm NCS} = 1.6$ reproduce the NIFS data with comparable quality and are in better agreement with $M/L_{\rm NCD} = 0.1$–0.25 estimated from integrated colours (see Section 2.1) than is $M/L_{\rm NCD} = 0.4$. Moreover, $M/L_{\rm NCD} = 0.1$ also agrees with the estimates from Bruzual & Charlot models (Bruzual & Charlot 2003).

The range of acceptable NCS masses is estimated as the range for which $\Delta\chi^2$ ($\Delta\chi^2_{\rm kin}$) is below 1σ confidence after 'marginalizing' over $M/L_{\rm NCD}$. Although $\Delta\chi^2$ is the more appropriate quantity to discriminate between models because both photometric and kinematic constraints are imposed on the models, the allowed NCS mass ranges determined using either $\Delta\chi^2$ or $\Delta\chi^2_{\rm kin}$ agree with each other. We obtain an NCS mass of $M_{\rm NCS} = 1.6^{+0.5}_{-0.2} \times 10^7\,{\rm M}_\odot$ within ≈42.4 pc. This is almost an order of magnitude higher than the lower limit of $\sim 2.5 \times 10^6\,{\rm M}_\odot$ obtained from the observed velocity of an H II region at a projected distance of 19 pc from the NC centre (Seth et al. 2006). The mass within ∼15 pc is $1.0 \times 10^7\,{\rm M}_\odot$, which agrees with the mass within the same radius obtained from the JAM models in H11, $(1.1 \pm 0.2) \times 10^7\,{\rm M}_\odot$. The mass of the NCD is not as well constrained: we obtain $3.6 \times 10^5\,{\rm M}_\odot$ for $M/L_{\rm NCD} = 0.1$ and $14.4 \times 10^5\,{\rm M}_\odot$ for $M/L_{\rm NCD} = 0.4$.

At this point models with 6M particles are constructed starting from the spherical isotropic 6M particle initial conditions. We start by generating high-resolution versions of models M1 with $M/L_{\rm NCD} = 0.1$. We again use photometric followed by photometric+kinematic constraints. But now we replace the FFT method with a spherical harmonics potential solver in order to obtain higher spatial resolution at the centre. These models also use a Runge–Kutta time-integrator with adaptive time-step [using routine ODEINT of Press et al. (1992) with accuracy parameter 10^{-6}] to allow a comparison with the models which include a black hole, presented in the next section. Since the potential is computed via an expansion in l, m spherical harmonics analogous to the photometric constraints, we include the same terms in the expansion of the potential as for the luminosity density (i.e. non-zero $A^{\rm NCD}_{lm}$ and $A^{\rm NCS}_{lm}$, cf. also Section 3.3). The potential is recalculated after every M2M correction step. We refer to the resulting models as series M2.

The 6M particle models illustrate several interesting points. The NCS mass estimated using 6M particles agrees with the estimates presented above using the M1 models. This suggests that the inferred NCS mass is robust with respect to how the models have been constructed, in particular to the potential solver, integration scheme and number of particles. Increasing the number of particles from M1 to M2 decreases $\chi^2_{\rm kin}$ of the corresponding best models by only a small amount (if at all) with respect to the $\Delta\chi^2_{\rm kin}$ confidence limit. This indicates that the model fitted to the NIFS data is dominated by the uncertainties in the data while the contribution of shot noise to $\chi^2_{\rm kin}$ is negligible. On the other hand, χ^2 is reduced considerably mainly due to a reduction in χ^2_{Alm}.[1] This suggests that χ^2_{Alm} is dominated by Poisson noise. Generally, $\chi^2_{Alm} < N_{Alm}$ because of the temporal smoothing, and both the M1 and M2 models reproduce the photometric data very well.

We present the intrinsic kinematics of the best-fitting model in series M2 in Fig. 4. We computed the radial, tangential and vertical dispersions, σ_u, σ_v and σ_w, respectively, and plot the anisotropies $\beta_\phi = 1 - (\sigma_v/\sigma_u)^2$ and $\beta_z = 1 - (\sigma_w/\sigma_u)^2$. In agreement with H11, we find that $\beta_z < 0$. Also $V_{\rm rms}$ has a central minimum. H11

[1] We use the same MC A_{lm} errors as for models M1.

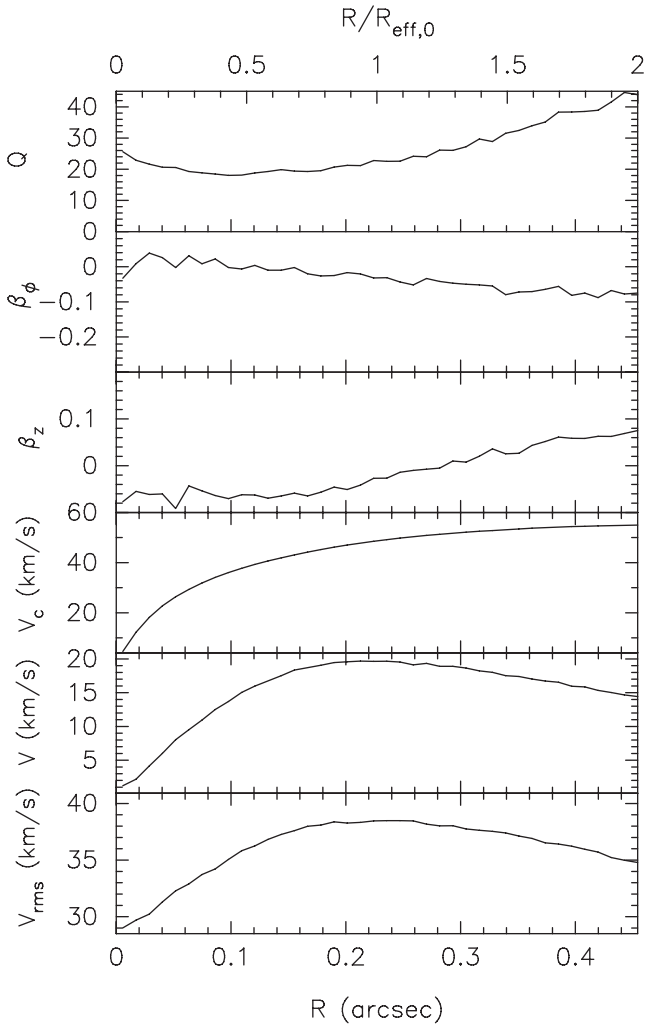

Figure 4. The intrinsic kinematics of the NC in the best-fitting model in the M2 series. From bottom to top, we show the second moment of line-of-sight velocity $V_{\rm rms}$, line-of-sight velocity V, the circular velocity V_c, the vertical anisotropy β_z and the tangential anisotropy β_ϕ. The top row shows the Toomre-Q of the NCD only.

found that the combination of these two properties provide important constraints on the amount of mass that the nuclear cluster could have accreted in the form of SCs, as we shall also see below.

4.1 Adding intermediate-mass black holes

Some galaxies are known to harbour both an NC and a massive black hole (Seth et al. 2008a; Graham & Spitler 2009; Neumayer & Walcher 2012). Since mass and anisotropy are degenerate with each other (Binney & Mamon 1982), we wish to explore how adding an IMBH might change β_z. We therefore also generate models including an IMBH at their centre with the aim of finding a robust upper IMBH mass limit compatible with the observations. We construct these models in a manner analogous to models M2 above, using a spherical harmonics potential solver in order to obtain higher spatial resolution at the centre. These models again use a Runge–Kutta time-integrator with adaptive time-step for higher accuracy in the vicinity of the IMBH. Using anisotropic JAM models (Cappellari 2008) H11 obtained an upper limit of $M_\bullet \lesssim 10^5\,{\rm M}_\odot$ on any black hole that may be present. We revisit this estimate with our more general three-integral modelling.

The IMBH is represented by a Plummer potential with scale-length set to 0.02 pc. We generate models M3 to M8 for various IMBH mass fractions. The IMBH mass fractions $\zeta = M_\bullet/(M/L_{\rm NCS} \times 10^5\,{\rm M}_\odot)$ are given in Table 2. For each series of models, the black hole mass is then given as $M_\bullet = \zeta \times M/L_{\rm NCS}$. The results of the models are presented in Fig. 5, which illustrates how the quality of the model fit changes with $M/L_{\rm NCS}$ and ζ. The left-hand panel shows $\Delta\chi^2 = \chi^2 - \min\{\chi^2\}$, whereas $\Delta\chi^2_{\rm kin}$ of the kinematic observables alone is shown in the middle and right-hand panels. The 68 per cent confidence limits are the same as given above, i.e. $\Delta\chi^2 = 68.8$ and $\Delta\chi^2_{\rm kin} = 27.0$.

As expected, the minimum χ^2 along a given line in Fig. 5 shifts towards smaller $M/L_{\rm NCS}$ with increasing IMBH mass fraction (see especially the right-hand panel of Fig. 5). Each line in Fig. 5 intersects the confidence limit (dashed horizontal line) twice (in the case of series M3 and M4 the modelling sets need to be extrapolated). The intersection with larger $M/L_{\rm NCS}$ corresponds to the largest admissible IMBH mass along each line. The largest IMBH mass compatible with the data would be obtained at a line that intersects the horizontal line only once, at its minimum χ^2. Using $\Delta\chi^2_{\rm kin}$ shown in the right-hand panel of Fig. 5, the dashed line with $M/L_{\rm NCS} = 1.2$ leads to the IMBH mass upper limit of $M_\bullet = 5.0 \times 10^5\,{\rm M}_\odot$. This upper limit is larger than the one found in H11 using JAM models, presumably reflecting the greater orbital freedom presented by three-integral versus less general anisotropic Jeans models.

If we use $\Delta\chi^2$ shown in the left-hand panel of Fig. 5 instead of $\Delta\chi^2_{\rm kin}$, we find that even larger IMBH masses (up to a factor 2 or higher) are compatible with the data. Nonetheless, we use the more conservative IMBH mass range provided by the NIFS data alone.

Fig. 6 shows a comparison of the best-fitting models in series M2 and M6 (indicated by the orange stars in the middle and right-hand panels of Fig. 5) with the integral-field NIFS kinematic. The model fits to the NIFS data are excellent. $\chi^2_{\rm kin}$ for the best models M2 and M6 are 194.715 and 207.532, respectively. Fig. 7 shows a comparison of the best-fitting models in the M2 and M6 series with major-axis kinematic data extracted from the NIFS data. The model kinematics are computed from a Gauss–Hermite fit to the line-of-sight velocity distribution in the corresponding Voronoi bins. To compute the temporally smoothed line-of-sight velocity distribution (LOSVD), we use 27 bins in velocity within a range of width 300 km s^{-1}, centred on the corresponding NIFS line-of-sight velocity. Note that we did not fit the full LOSVD itself, instead we constrained the particle models using luminosity-weighted moments as described in Section 3.1.

5 *N*-BODY SIMULATIONS

Our best dynamical model without an IMBH is M2 with $M/L_{\rm NCS} = 1.5$. After building this model, we used it for a number of N-body experiments testing its stability and evolution by using it as initial conditions. The simulations were evolved with PKDGRAV (Stadel 2001), an efficient, multistepping, parallel treecode. In all cases, we use an opening angle $\theta = 0.7$. We used base time-step $\Delta t = 0.1$ Myr and changed time-steps of individual particles such that $\delta t = \Delta t/2^n < \eta(\epsilon/a)^{1/2}$, where ϵ is the softening and a is the acceleration of the particle, with n as large as 29 allowed. We set $\eta = 0.03$, a quite conservative value.

5.1 Stability test

In constructing our dynamical model, we have assumed that the NC in NGC 4244 is very likely axisymmetric. H11 found no evidence of non-axisymmetry in the NC of M33. Its PA is consistent with that

Table 2. Summary of the modelling runs. Columns from left to right are: name of the series of models, number of particles, mass-to-light ratio of the NCD, mass-to-light ratio of the NCS, IMBH mass fraction ζ, the method used to compute the potential and the time integration scheme.

Series	N_p ($\times 10^6$)	$M/L_{\rm NCD}$	$M/L_{\rm NCS}$	$\zeta = \frac{M_{\rm BH}}{(M/L_{\rm NCS})\times 10^5\,{\rm M}_\odot}$	Pot.	Int.
M1	0.75	0.1, 0.2, 0.4	1.0–4.8	–	FFT	Leapfrog
M2	6	0.1	1.0–2.2	–	Sph. harm.	Runge–Kutta
M3	6	0.1	1.1–1.5	0.6	Sph. harm.	Runge–Kutta
M4	6	0.1	1.1–1.5	0.9	Sph. harm.	Runge–Kutta
M5	6	0.1	1.1–1.5	1.2	Sph. harm.	Runge–Kutta
M6	6	0.1	1.2–1.4	2.3	Sph. harm.	Runge–Kutta
M7	6	0.1	1.0–1.3	3.5	Sph. harm.	Runge–Kutta
M8	6	0.1	1.0–1.4	5.8	Sph. harm.	Runge–Kutta

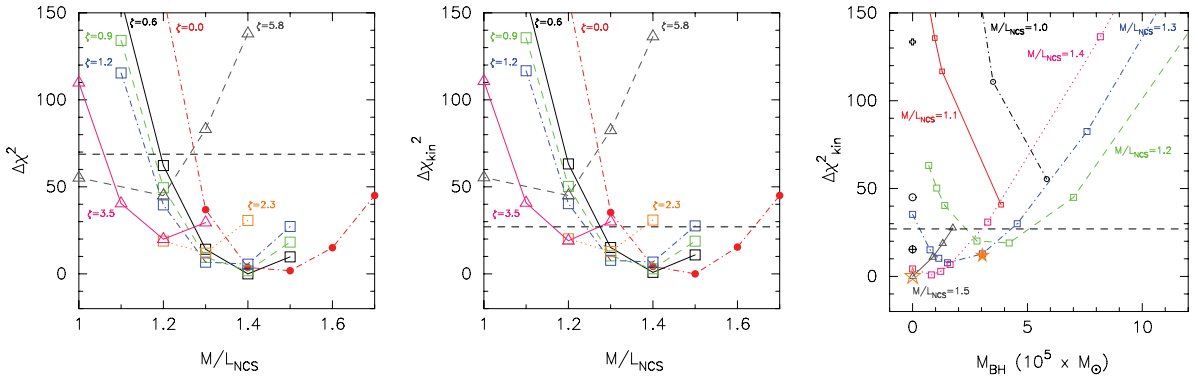

Figure 5. $\Delta\chi^2 = \chi^2 - \min\{\chi^2\}$ as a function of NCS mass-to-light ratio for various IMBH mass fractions $\zeta = M_\bullet/(M/L_{\rm NCS})$. Left-hand panel: total $\Delta\chi^2$ for the model fitted to the photometric and kinematic target observables. Middle panel: $\Delta\chi^2_{\rm kin}$ of the kinematic observables only. Right-hand panel: $\Delta\chi^2_{\rm kin}$ as a function of $M_\bullet$ instead of $M/L_{\rm NCS}$. The dashed horizontal lines correspond to 68 per cent (1σ) confidence after van den Bosch & van de Ven (2009). In the left-hand and middle panels, the symbols are as follows: the M2 series is shown as solid (red) circles joined by red dot–dashed lines. Models including a central IMBH are shown as open squares joined by (black) solid (M3), (green) dashed (M4), (blue) dot–dashed (M5) or (orange) dotted (M6) lines. The open triangles are for series M7 and M8. The M7 and M8 series are joined by (pink) solid and (grey) dashed lines, respectively. IMBH mass fractions for models in the M3–M8 series are given in Table 2. In the right-hand panel, the different symbols represent – circles joined by (black) dot–dashed line: $M/L_{\rm NCS} = 1$, squares joined by (red) solid line: $M/L_{\rm NCS} = 1.1$, squares joined by (green) dashed line: $M/L_{\rm NCS} = 1.2$, squares joined by (blue) dot–dashed line: $M/L_{\rm NCS} = 1.3$, squares joined by (pink) dotted line: $M/L_{\rm NCS} = 1.4$, triangles joined by (grey) solid line: $M/L_{\rm NCS} = 1.5$, (single) crossed circle: $M/L_{\rm NCS} = 1.6$, (single) dotted circle: $M/L_{\rm NCS} = 1.7$, (single) cross: $M/L_{\rm NCS} = 1.9$ and (single) diamond: $M/L_{\rm NCS} = 2.2$. The open and solid (orange) stars in the middle and right-hand panels mark the best-fitting M2 and M6 models, respectively.

of its MD and its apparent ellipticity is consistent with a vertical flattening of $q = 0.7$, the average observed in the NCs of edge-on late-type galaxies (Seth et al. 2006). There is also only a small misalignment between the photometric and the kinematic major axes. At present, M33 is the only galaxy in which the axial symmetry of the NC can be determined.

Our first N-body simulation therefore tests the stability of the model against non-axisymmetric perturbations, particularly the bar instability, which plagues rapidly rotating systems. After evolving the best-fitting model in series M2 for 50 Myr (the rotation period at 5 pc being 0.63 Myr), the model remained axisymmetric with no hint of a bar or spirals. The top panel of Fig. 4 plots the Toomre-$Q = \sigma_u\kappa/(3.36G\Sigma)$ of the NCD, where κ is the epicyclic radial frequency, G is the gravitational constant and Σ is the surface density. The stability of the system stems from the high Toomre-Q of the NCD, which is everywhere greater than 10.

5.2 Accretion simulations

H11 explored the hypothesis that NC formation is a result of SC accretion. They showed that the observed kinematics of the NC in NGC 4244 are not consistent with accretion of more than ∼50 per cent of its mass in the form of SCs. Specifically, once the accreted mass fraction exceeded this value the resulting central $V_{\rm rms}$ was no longer a minimum. We will see here too that $V_{\rm rms}$ starts to lose its central minimum once the accreted mass fraction becomes too large, and our constraint is even more stringent than that of H11. On the other hand, H11 showed that the negative β_z of the NC was only possible if it accreted $\gtrsim$10 per cent of its mass as SCs on highly inclined orbits. Those simulations assumed SCs accreting on to a pre-existing NC, either as an NCD or as an isotropic NCS. Therefore, we next subject our best-fitting model of the NC to SC accretions.

In order to permit the model SCs to sink to the centre via dynamical friction, we introduce the best-fitting model in the M2 series inside a particle MD with an exponential profile, because NGC 4244 is a late-type, bulgeless galaxy. We use the same model for the MD as did H11, i.e. four million multimass particles with masses ranging from 7 $\rm M_\odot$ within the inner 20 pc increasing to 1.2×10^7 $\rm M_\odot$ in the disc outskirts. The distributions of masses and softening of the MD particles are shown in fig. 6 of H11; the softening is related to particle mass via $\epsilon_p \propto m_p^{1/3}$.

We accrete three of the model SCs described in H11 which we term G1, G2 and G3 in order of increasing mass. Their properties

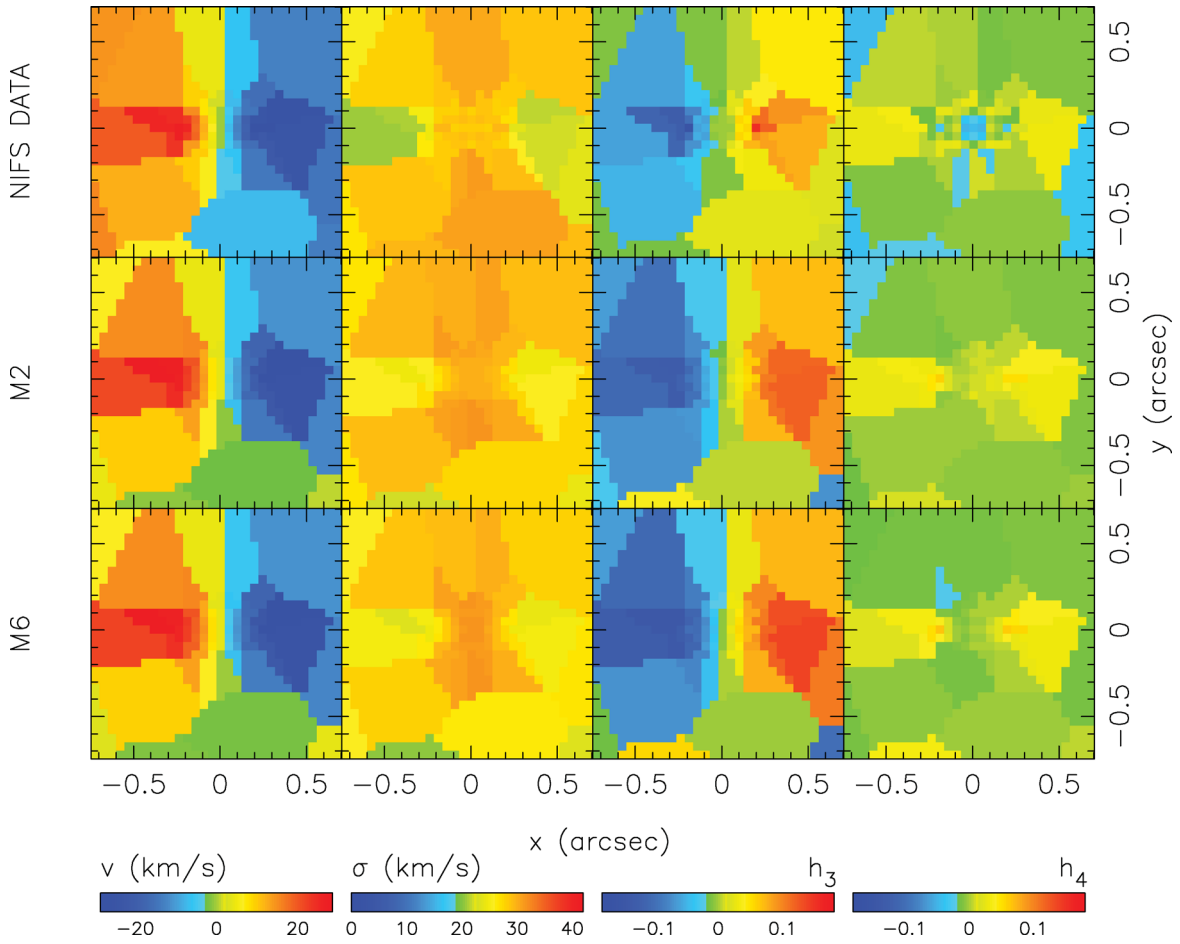

Figure 6. Symmetrized NIFS integral-field kinematic data within ±0.7 arcsec of the central region of NGC 4244 (top row) compared with corresponding luminosity-weighted data extracted from the best-fitting models in series M2 (middle row) and M6 with $M/L_{\rm NCD} = 0.1$, $M/L_{\rm NCS} = 1.3$ and $M_\bullet = 3.0 \times 10^5$ M$_\odot$ (bottom row). These models are indicated by the open and solid orange stars, respectively, in the right-hand panel of Fig. 5. From left to right are shown: line-of-sight velocity v, line-of-sight velocity dispersion σ and higher order Gauss–Hermite moments h_3 and h_4.

are listed in Table 3. As in H11, we define the concentration of each SC as $c \equiv \log(R_{\rm eff}/R_c)$, where $R_{\rm eff}$ is the half-mass radius (effective radius) and R_c is the core radius, where the surface density drops to half of the central. These were allowed to accrete on to the NC starting from circular orbits at 50 pc from the centre. We start the SCs from four different inclinations relative to the NCD: 0°, 30°, 60° and 90°. The SCs require about 40 Myr to accrete on to the NC.

The results of these accretion simulations are shown in Fig. 8. The low-density SC G1 is disrupted at ∼8 pc from the centre. Thus, it barely perturbs the kinematics of the NC. However, we note that there is a general tendency for β_z to increase slightly within $R_{\rm eff}$, suggesting that even this mild ∼1 per cent mass accretion can alter the kinematics. The more massive, denser, clusters G2 and G3, both of which sink all the way to the centre, perturb the kinematics much more. In all the cases β_z increases; for G2 β_z averaged within $R_{\rm eff}$ is nearly zero, while $\beta_z > 0$ everywhere within $R_{\rm eff}$ when G3 is accreted.

Accreting G3 (which has a mass ∼13 per cent that of the NC) also raises the central $V_{\rm rms}$. Although $V_{\rm rms}$ at the centre remains smaller than at $R_{\rm eff}$, there does not seem to be much room for further significant accretions without making $V_{\rm rms}$ centrally peaked, unlike the observations. This is likely to hold also if this mass fraction arrives as many smaller SCs, provided that the SCs are dense enough that some fraction of their stars survives all the way to the centre of the NC.

6 DISCUSSION AND CONCLUSIONS

We have performed a dynamical study of the nuclear cluster in the edge-on spiral galaxy NGC 4244 taking into account different morphological components, which are the galaxy MD, NCD and NCS. We have constructed axisymmetric dynamical particle models accounting for the MD, the NCD and the NCS. We find a total NCS mass $M_{\rm NCS} = 1.6^{+0.5}_{-0.2} \times 10^7$ M$_\odot$ within approximately 42.4 pc (2 arcsec). Both the fits of Seth et al. (2005a) and Fry et al. (1999) show that there is no obvious bulge component in NGC 4244. Using the 2MASS Large Galaxy Atlas (Jarrett et al. 2003) K-band magnitude, the total luminosity of the galaxy is 3.2×10^9 L$_\odot$, and thus the galaxy stellar mass is 2×10^9 M$_\odot$. Fig. 9 plots the NC mass compared with the $M_{\rm CMO}$–$M_{\rm gal}$ relation. The NC sits above this relation.

6.1 Vertical anisotropy

The kinematics are moderately tangentially anisotropic inside $R_{\rm eff}$ with an anisotropy parameter $\beta_z \sim -0.1$. This is in good agreement

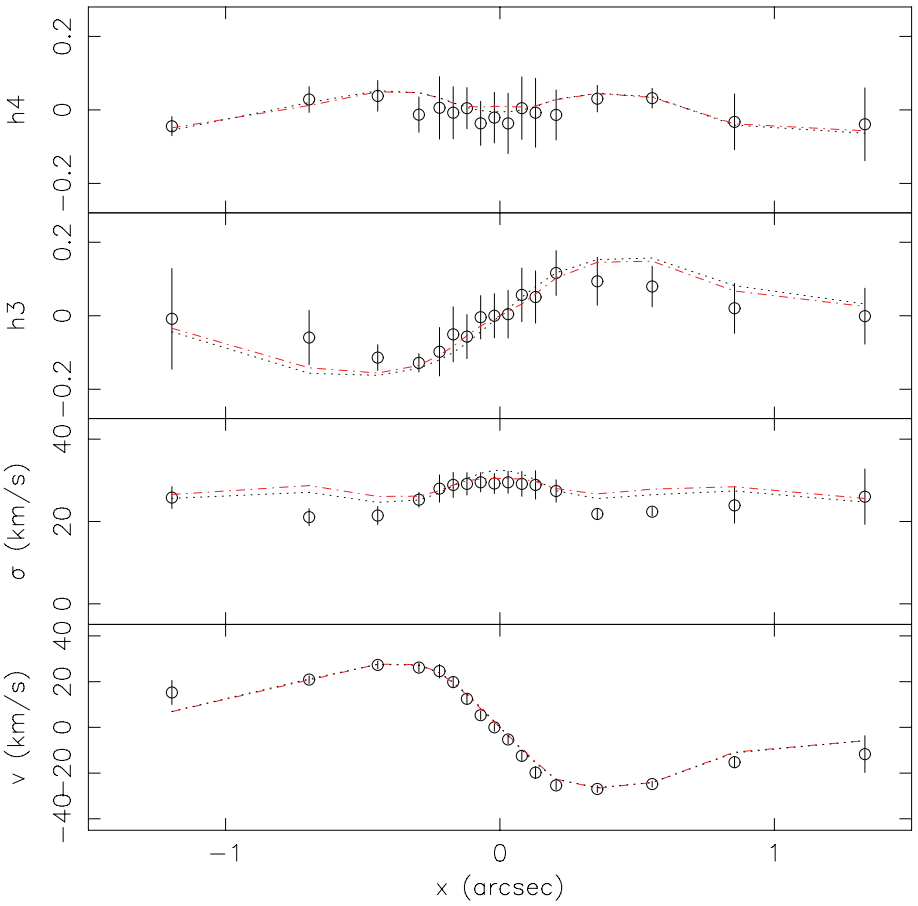

Figure 7. Comparison of the best-fitting models in series M2 and M6 (indicated by the open and solid orange stars in Fig. 5) to the kinematic data along the major axis extracted from the NIFS data. Models and data are shown as lines and open circles, respectively, with M2 indicated by the dot–dashed (red) line and M6 by the dotted (black) line. From bottom to top are shown: velocity v, velocity dispersion σ and Gauss-Hermite moments h_3 and h_4. The model kinematic data were computed using a Gauss–Hermite fit to the velocity distribution along the line of sight.

Table 3. The SCs used in the accretion simulations. $M_\star$ is the stellar mass of the SC, $R_{\rm eff}$ is the effective (half-mass) radius and c is the concentration (defined in the text). For comparison, the last column lists the name used for the model in H11.

Model	$M_\star$ ($\times 10^5$ M$_\odot$)	$R_{\rm eff}$ (pc)	c	H11 name
G1	2	1.11	0.12	C4
G2	6	1.11	0.16	C5
G3	20	2.18	0.12	C3

with the JAM models of H11. H11 showed that $\beta_z < 0$ requires high-inclination infall of SCs on to a pre-existing nuclear cluster. In our accretion simulations on to a more realistic model of the NC, we found that even the accretion of an SC of just 13 per cent, the mass is enough to erase the vertical anisotropy. This raises questions about whether such anisotropy can be due to accretion at all. It also hints that, unless we are observing the NC of NGC 4244 at a special time, it cannot sustain accretion of $\gtrsim$10 per cent mass as suggested by H11.

We therefore tested whether the assumption of a perfectly edge-on nuclear cluster may bias the modelled vertical anisotropy to negative values if the real inclination is somewhat smaller. The smallest inclination at which we were able to deproject the NCD photometry was 83°. Using a model deprojected at this assumed inclination and the observed kinematics, we built NMAGIC models assuming $M/L_{\rm NCS} = 1.5$ starting from the best-fitting edge-on model M2. The dashed black lines in Fig. 10 show that the 2D anisotropy, $\beta_z = 1 - \sigma_z^2/\sigma_R^2$, and 3D anisotropy, $B_z = 1 - 2\sigma_z^2/(\sigma_R^2 + \sigma_\phi^2)$, are barely changed compared to the edge-on case (solid black lines) and remain negative. Thus, a negative vertical anisotropy is not an artefact of assuming that the nuclear cluster is perfectly edge-on.

We finally explore whether the recovered β_z changes if we include IMBHs in the models. In Fig. 10, we plot both the vertical anisotropies for varying $M_\bullet$. While increasing $M_\bullet$ raises the vertical anisotropy, it still remains negative within $R_{\rm eff}$. We conclude that the NC must be vertically anisotropic even if a black hole were present.

6.2 Summary

We have built dynamical models of the NC in the nearby, edge-on late-type galaxy NGC 4244. Using particle re-sampling, we were able to obtain a narrow distribution of weights in our NMAGIC models allowing us to use the models as initial conditions in N-body simulations. Our results can be summarized as follows.

(i) We find a mass of the spheroidal component of the NC, $M_{\rm NCS} = 1.6^{+0.5}_{-0.2} \times 10^7$ M$_\odot$ within 42.4 pc. The mass within 15 pc is $\sim$1.0 $\times 10^7$ M$_\odot$, in very good agreement with the value estimated

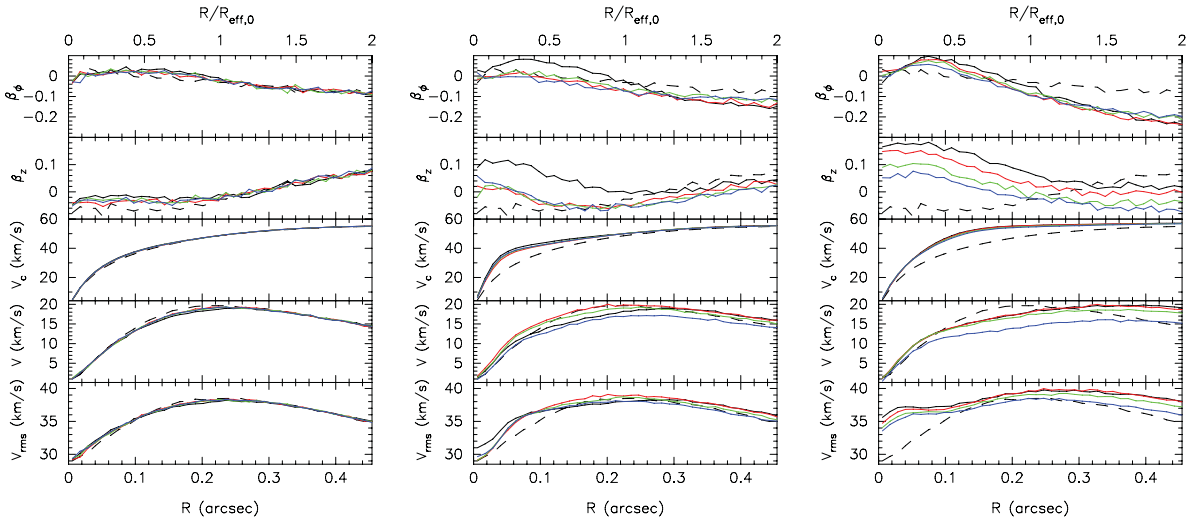

Figure 8. The effect of accreting SCs on to the NC in NGC 4244. From left to right these show the effect of accreting SCs G1, G2 and G3. The black, red, green and blue solid lines show SCs accreting from 0°, 30°, 60° and 90°, respectively. The dashed line shows the initial NC.

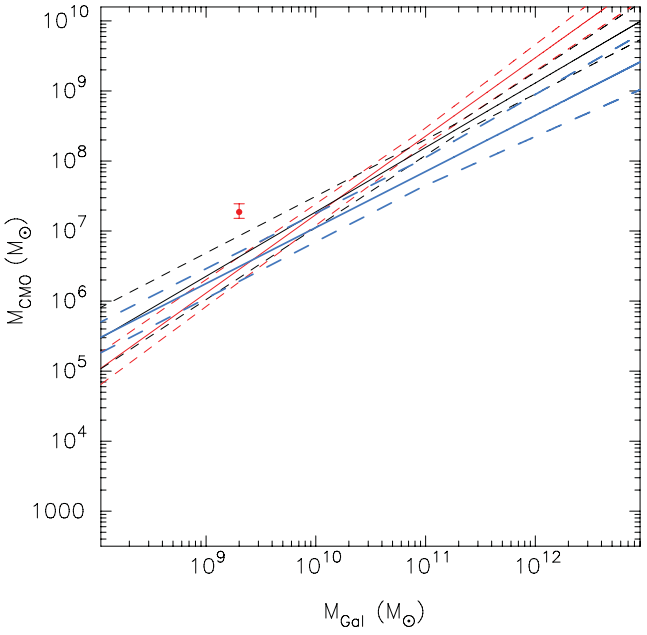

Figure 9. Mass of the NC of NGC 4244 versus the mass of the host galaxy compared with the $M_{\rm CMO}$–$M_{\rm gal}$ relations of Ferrarese et al. (2006). The solid red and black lines show the correlations for NCs and SMBHs in early-type galaxies, respectively, with 1σ confidence levels shown as dashed lines. The blue lines show the relation of Scott & Graham (2012).

by H11 using anisotropic JAM models. This mass puts the nuclear cluster above the $M_{\rm NC}$–$M_{\rm Gal}$ relation.

(ii) The mass of the bluer disc component of the nuclear cluster is less constrained and covers the range $3.6 \times 10^5 \lesssim M_{\rm NCD} \lesssim 14.4 \times 10^5\,{\rm M}_\odot$.

(iii) Our three-integral models are consistent with no black hole as well as with a black hole as massive as $4.6 \times 10^5\,{\rm M}_\odot$. This upper limit is larger than the one allowed by anisotropic JAM models.

(iv) Simulations show that the model without a black hole is stable against axisymmetric perturbations. This stability is derived from the large Toomre-Q of the system.

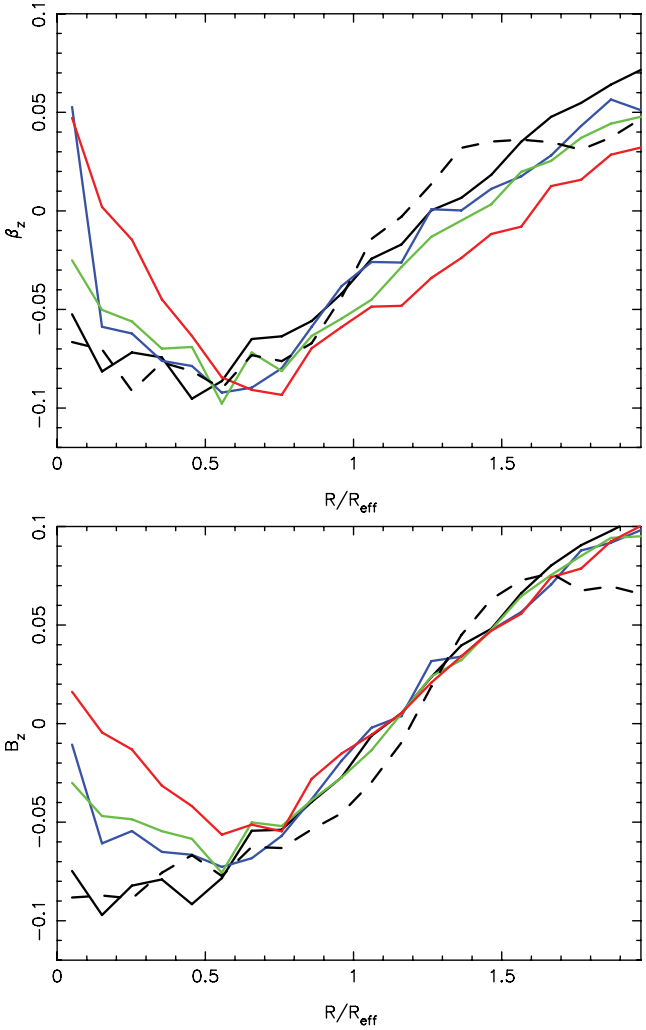

Figure 10. Profiles of 2D (top) and 3D (bottom) vertical anisotropy. The black, blue, green and red lines correspond to $M_\bullet = 0$, 0.8, 1.23 and $3.0 \times 10^5\,{\rm M}_\odot$, respectively. The dashed lines correspond to assuming that the nuclear cluster is inclined at 83° instead of being perfectly edge-on.

(v) Regardless of whether a black hole is present or not, and whether the nuclear cluster is perfectly edge-on or not, β_z and B_z are both negative. Accretion of an SC of as little as 13 per cent by mass is enough to drive β_z to positive values, regardless of the orbital geometry. It remains unclear, therefore, how $\beta_z < 0$ arose.

ACKNOWLEDGMENTS

The NMAGIC models in this paper were run on Albert, the supercomputer at the University of Malta. The simulations were run on Albert, on the High Performance Computer Facility at the University of Central Lancashire and on the COSMOS Consortium supercomputer within the DIRAC Facility jointly funded by STFC, the Large Facilities Capital Fund of BIS. Additional low-resolution test models were run on the old linux cluster of the dynamics group at MPE. VPD is supported in part by STFC Consolidated grant no. ST/J001341/1.

REFERENCES

Adams F. C., Graff D. S., Richstone D. O., 2001, ApJ, 551, L31
Adams F. C., Graff D. S., Mbonye M., Richstone D. O., 2003, ApJ, 591, 125
Agarwal M., Milosavljević M., 2011, ApJ, 729, 35
Antonini F., 2012, arXiv:1207.6589
Antonini F., Capuzzo-Dolcetta R., Mastrobuono-Battisti A., Merritt D., 2012, ApJ, 750, 111
Bekki K., 2007, PASA, 24, 77
Bekki K., Couch W. J., Shioya Y., 2006, ApJ, 642, L133
Bell E. F., McIntosh D. H., Katz N., Weinberg M. D., 2003, ApJS, 149, 289
Binney J., Mamon G. A., 1982, MNRAS, 200, 361
Böker T., Laine S., van der Marel R. P., Sarzi M., Rix H.-W., Ho L. C., Shields J. C., 2002, AJ, 123, 1389
Böker T., Sarzi M., McLaughlin D. E., van der Marel R. P., Rix H.-W., Ho L. C., Shields J. C., 2004, AJ, 127, 105
Bruzual G., Charlot S., 2003, MNRAS, 344, 1000
Burkert A., Silk J., 2001, ApJ, 554, L151
Cappellari M., 2008, MNRAS, 390, 71
Capuzzo-Dolcetta R., Miocchi P., 2008, MNRAS, 388, L69
Côté P. et al., 2006, ApJS, 165, 57
Davidge T. J., Courteau S., 2002, AJ, 123, 1438
de Lorenzi F., Debattista V. P., Gerhard O., Sambhus N., 2007, MNRAS, 376, 71
de Lorenzi F., Gerhard O., Saglia R. P., Sambhus N., Debattista V. P., Pannella M., Méndez R. H., 2008, MNRAS, 385, 1729
de Lorenzi F. et al., 2009, MNRAS, 395, 76
Debattista V. P., Sellwood J. A., 2000, ApJ, 543, 704
Dehnen W., 2009, MNRAS, 395, 1079
Di Matteo T., Springel V., Hernquist L., 2005, Nat, 433, 604
Erwin P., Gadotti D., 2010, in Debattista V. P., Popescu C. C., eds, AIP Conf. Ser. Vol. 1240, Am. Inst. Phys., New York, p. 223
Erwin P., Gadotti D. A., 2012, Advances in Astronomy, Vol. 2012, Article ID 946368
Ferrarese L. et al., 2006, ApJ, 644, L21
Fry A. M., Morrison H. L., Harding P., Boroson T. A., 1999, AJ, 118, 1209
Gebhardt K. et al., 2000, ApJ, 539, L13
Gerhard O. E., 1991, MNRAS, 250, 812
Gerhard O. E., 1993, MNRAS, 265, 213
Graham A. W., 2012, MNRAS, 422, 1586
Graham A. W., Spitler L. R., 2009, MNRAS, 397, 2148
Graham A. W., Onken C. A., Athanassoula E., Combes F., 2011, MNRAS, 412, 2211
Greene J. E. et al., 2010, ApJ, 721, 26
Haehnelt M. G., Kauffmann G., 2000, MNRAS, 318, L35
Hartmann M., Debattista V. P., Seth A., Cappellari M., Quinn T. R., 2011, MNRAS, 418, 2697 (H11)
Hockney R. W., Eastwood J. W., 1988, Computer Simulation Using Particles. Adam Hilger, Bristol
Jahnke K., Macciò A. V., 2011, ApJ, 734, 92
Jarrett T. H., Chester T., Cutri R., Schneider S. E., Huchra J. P., 2003, AJ, 125, 525
Johansson P. H., Naab T., Burkert A., 2009, ApJ, 690, 802
Kazantzidis S. et al., 2005, ApJ, 623, L67
King A., 2003, ApJ, 596, L27
Leigh N., Böker T., Knigge C., 2012, MNRAS, 424, 2130
Lotz J. M., Telford R., Ferguson H. C., Miller B. W., Stiavelli M., Mack J., 2001, ApJ, 552, 572
Magorrian J., 1999, MNRAS, 302, 530
McLaughlin D. E., King A. R., Nayakshin S., 2006, ApJ, 650, L37
Milosavljević M., 2004, ApJ, 605, L13
Miralda-Escudé J., Kollmeier J. A., 2005, ApJ, 619, 30
Murray N., Quataert E., Thompson T. A., 2005, ApJ, 618, 569
Neumayer N., Walcher C. J., 2012, Advances in Astronomy, Vol. 2012, Article ID 709038 (arXiv:1201.4950)
Paturel G. et al., 1995, in Egret D., Albrecht M. A., eds, LEDA: the Lyon-Meudon Extragalactic Database, Astrophysics and Space Science Library, Vol. 203, p. 115
Press W. H., Teukolsky S. A., Vetterling W. T., Flannery B. P., 1992, Numerical recipes in FORTRAN. The art of scientific computing, 2nd edn. Cambridge Univ. Press, Cambridge
Rossa J., van der Marel R. P., Böker T., Gerssen J., Ho L. C., Rix H.-W., Shields J. C., Walcher C.-J., 2006, AJ, 132, 1074
Rybicki G. B., 1987, in de Zeeuw P. T., Tremaine S. D., eds, Structure and Dynamics of Elliptical Galaxies, Proc. IAU Symp. 127, held 27–31 May 1986 in Princeton, NJ. Reidel, Dordrecht, p. 397
Sazonov S. Y., Ostriker J. P., Ciotti L., Sunyaev R. A., 2005, MNRAS, 358, 168
Schinnerer E., Böker T., Meier D. S., 2003, ApJ, 591, L115
Scott N., Graham A. W., 2012, arXiv:1205.5338
Sellwood J. A., 2003, ApJ, 587, 638
Sérsic J. L., 1968, Atlas de galaxias australes. Observatorio Astronomico, Cordoba
Seth A. C., Dalcanton J. J., de Jong R. S., 2005a, AJ, 129, 1331
Seth A. C., Dalcanton J. J., de Jong R. S., 2005b, AJ, 130, 1574
Seth A. C., Dalcanton J. J., Hodge P. W., Debattista V. P., 2006, AJ, 132, 2539
Seth A., Agüeros M., Lee D., Basu-Zych A., 2008a, ApJ, 678, 116
Seth A. C., Blum R. D., Bastian N., Caldwell N., Debattista V. P., 2008b, ApJ, 687, 997
Silk J., Rees M. J., 1998, A&A, 331, L1
Springel V., Di Matteo T., Hernquist L., 2005, MNRAS, 361, 776
Stadel J. G., 2001, PhD thesis, Univ. Washington
Syer D., Tremaine S., 1996, MNRAS, 282, 223
Tremaine S. D., Ostriker J. P., Spitzer L., Jr, 1975, ApJ, 196, 407
van den Bosch R. C. E., van de Ven G., 2009, MNRAS, 398, 1117
van der Kruit P. C., Searle L., 1981, A&A, 95, 105
van der Marel R. P., Franx M., 1993, ApJ, 407, 525
Walcher C. J., Böker T., Charlot S., Ho L. C., Rix H.-W., Rossa J., Shields J. C., van der Marel R. P., 2006, ApJ, 649, 692
Wehner E. H., Harris W. E., 2006, ApJ, 644, L17

This paper has been typeset from a TEX/LATEX file prepared by the author.